ATLAS PUB Note

ATL-PHYS-PUB-2018-012

13th July 2018

Track assisted techniques for jet substructure

The ATLAS Collaboration

The substructure of large-radius (large-R) jets provides an important handle to discriminate hadronic decays such as $W \to qq$, $H \to bb$, $H \to W(qq)W^*(qq)$, and $t \to W(qq)b$ from QCD multijet backgrounds. Three algorithms that combine tracking and calorimeter information to calculate large-R jet substructure observables are presented. The first algorithm makes use of both subjets and associated tracks to calculate new observables for standard large-R jets. The other two newly developed algorithms use tracks and small-R jets to construct new large-R jets with observables that make use of information from both sets of inputs. These techniques are shown to improve the discrimination power of signal jets from background relative to the current ATLAS large-R jet reconstruction techniques.

ATL-PHYS-PUB-2018-012
13 July 2018

1 Introduction

As analyses of ATLAS data probe higher kinematic regimes, highly boosted heavy particles become increasingly relevant and accessible. In the case that these particles decay hadronically, e.g., a W boson decaying as $W \to qq$, a Higgs boson decaying as $H \to bb$ or $H \to W(qq)W^*(qq)$, or a top quark decaying as $t \to W(qq)b$, the resulting hadronic showers overlap and it becomes necessary to use large-R jets to reconstruct the decay products[1]. In the following, large-R jets from hadronic W boson, $H \to bb$, $H \to WW^*$, and top quark decays are referred to as W, $H \to bb$, $H \to WW^*$, and top jets, respectively. The distribution of energy inside a jet, commonly referred to as "jet substructure" [1, 2], contains information about the initiating particle, such as its mass and decay pattern. The precise reconstruction of jet substructure is instrumental to the discrimination of W, Higgs, and top jets against multijet background jets, originating from gluons or light quarks and referred to as QCD jets throughout this document. Given the similarity between hadronic $W \to qq$ and $Z \to qq$ decays, the conclusions obtained using W jets also apply to the identification of $Z \to qq$ decays.

The reconstruction of jet substructure observables becomes more challenging as the transverse momentum of jets increases due to the stronger collimation of the decay products. This effect is driven by the finite angular resolution of the ATLAS calorimeter, which is typically used to reconstruct jet substructure observables [3]. This limitation can be overcome by using additional information from tracks reconstructed in the inner detector, which provides a good angular resolution for charged jet components. Since the tracker is not sensitive to neutral jet components, the momentum scale of the tracks from charged particles can be corrected or "assisted" [4, 5] using calorimeter information. The simplest method of applying this correction is with the total p_{T} of the large-R jet, as is done for the jet mass observable m^{TA} [3], which is used as an input for the current ATLAS jet mass definition. The performance can be further improved by applying local corrections when assisting tracks. For instance, this can be done by using the p_{T} of each k_t subjet of a large-R jet, resulting in m^{TAS} [3], or the p_{T} of each cluster of energy deposits in the calorimeter with the Track-CaloCluster method [6]. An alternative is the particle flow approach [7], which removes calorimeter energy deposits due to charged hadrons from consideration during jet reconstruction, instead using measurements of their momenta from the tracker.

This document presents two novel approaches extending the track-assisted subjet (TAS) method. They use anti-k_t $R = 0.2$ jets reconstructed from energy deposits in the calorimeters to reconstruct large-R jets and to determine local corrections to the p_{T} of nearby tracks. The advantage of this approach over the track-assistance methods presented above is that it benefits from dedicated calibration applied to the anti-k_t $R = 0.2$ input jets. The performance of the two novel approaches is studied in several regions of phase space, and it is shown that track-assisted jet substructure observables have better resolutions than observables calculated from only calorimeter information, and provide an improved separation from QCD jets.

A description of the ATLAS detector is given in Section 2 and an overview of the simulated samples used in this study is given in Section 3. The physics objects and substructure observables used in this study are defined in Section 4. The track-assisted jet substructure methods are described in detail in Section 5. The performance of the track-assisted methods, in terms of the resolution of observables and effectiveness in tagging heavy resonances, is compared to other existing approaches in Section 6. Finally, the conclusions of this document are presented in Section 7.

[1] Throughout this document, simplified notation is used, e.g., $W \to q'\bar{q}$ is denoted as $W \to qq$.

2 The ATLAS detector

The ATLAS experiment is a multi-purpose detector located at the LHC at CERN. It has a forward-backward symmetric cylindrical geometry with a nearly 4π solid angle coverage[2]. It consists of an inner detector (ID) tracking system, electromagnetic (EM) and hadronic calorimeters, a muon spectrometer (MS) and a magnet system. The ID consists of a silicon pixel and strip layers that extend to $|\eta| < 2.5$ and straw tube transition radiation tracker detectors that cover $|\eta| < 2.0$. A thin solenoid magnet surrounds the ID to provide the strong magnetic field necessary to measure the momentum and charge of electrically charged particles. The central calorimeter system consists of a lead/liquid-argon (LAr) sampling EM calorimeter, which is split into barrel ($|\eta| < 1.5$) and endcap ($1.5 < |\eta| < 3.2$) sections, and a sampling hadronic calorimeter which is subdivided into a steel/scintillating-tile barrel region ($|\eta| < 1.7$) and two copper/liquid-argon endcap regions ($1.5 < |\eta| < 3.2$). The forward region ($3.1 < |\eta| < 4.9$) is covered by a liquid-argon calorimeter with Cu (W) absorber in the EM (hadronic) layer(s). The MS consists of a system of precision gaseous tracking chambers and three large toroid magnet systems designed to allow the measurement of muon charge and momentum.

3 Simulated samples

Simulated Monte Carlo (MC) samples are produced for five different jet topologies. Dijet samples used to study QCD jets, Sequential Standard Model $W' \to W(qq)Z(qq)$ samples for W jets, and Sequential Standard Model $Z' \to tt$ samples for top jets are generated using Pythia8 [8] with the NNPDF2.3LO PDF set [9] with the A14 underlying event tune [10]. The dijet samples are produced in p_{T} slices and are reweighted to produce the physical jet p_{T} spectrum. The W' samples have a mass range of 600 GeV $\leq m_{W'} \leq$ 5 TeV and the Z' samples have a mass range of 1 TeV $\leq m_{Z'} \leq$ 5 TeV. Samples consisting of a Kaluza-Klein graviton [11, 12] decaying as $G^*_{KK} \to H(bb)H(bb)$ are used to study $H \to bb$ jets and are generated using MadGraph5_aMC@NLO [13] interfaced with Pythia8 for parton showering, hadronization, and underlying event simulation with the NNPDF2.3LO PDF set and the A14 underlying event tune. These are produced with a mass range of 600 GeV $\leq m_{G^*_{KK}} \leq$ 6 TeV. Samples of a heavy neutral scalar decaying as $X \to H(WW^*)H(WW^*)$, where all W bosons are required to decay hadronically, are used to study $H \to WW^*$ jets and are generated using MadGraph5_aMC@NLO interfaced with Herwig++ [14] for parton showering with the CTEQ6L1 PDF set [15] and the UEEE5 underlying event tune [16]. These are produced with a mass range of 1 TeV $\leq m_X \leq$ 3 TeV.

Additional interactions within the same or neighboring bunch crossings (pile-up) can alter the measured energy of jets or lead to the reconstruction of additional, spurious jets. Their effect on reconstructed jets is modelled by overlaying multiple low-energy inelastic proton-proton events on the signal hard-scatter event. These events are generated with Pythia8. The distribution of the number of interactions in simulation is weighted to match the mean interactions per bunch crossing of 22 in the combined data collected in 2015 and 2016.

All MC samples are processed through the full ATLAS detector simulation [17] based on Geant4 [18].

[2] ATLAS uses a right-handed coordinate system with its origin at the nominal interaction point (IP) in the center of the detector and the z-axis along the beam pipe. The x-axis points from the IP to the center of the LHC ring, and the y-axis points upwards. Cylindrical coordinates (r, ϕ) are used in the transverse plane, ϕ being the azimuthal angle around the z-axis.The pseudorapidity is defined in terms of the polar angle θ as $\eta = -\ln\tan(\theta/2)$. Angular distance is measured in units of $\Delta R \equiv \sqrt{(\Delta\eta)^2 + (\Delta\phi)^2}$.

4 Definition of objects and standard jet substructure observables

4.1 Tracks

Tracks are reconstructed using hits in the inner detector. In order to ensure that only well-reconstructed tracks from the hard interaction are used, requirements on the number of hits and impact parameters relative to the primary vertex of the hard interaction are applied [19, 20], as detailed in Ref. [3]. Only tracks with $p_{\mathrm{T}} > 500$ MeV and $|\eta| < 2.5$ are used. The primary vertex is selected as the vertex with the highest scalar p_{T}^2 sum of tracks associated with it using transverse and longitudinal impact parameter requirements.

4.2 $R = 0.2$ jets

$R = 0.2$ jets are constructed from locally calibrated topological clusters [21] using the FastJet [22] implementation of the anti-k_t algorithm [23] with a radius parameter of $R = 0.2$. MC-based calibrations are derived and applied following the same scheme as described in Ref. [24] for $R = 0.4$ jets, which account for the residual pile-up dependence and the absolute jet energy scale, and apply a global sequential correction using tracks and muon segment information. Furthermore, $R = 0.2$ jets are required to have $p_{\mathrm{T}} > 20$ GeV and to fall within $|\eta| < 2.5$.

4.3 Large-R jets

Standard large-R jets are reconstructed from locally calibrated topological clusters using the FastJet implementation of the anti-k_t algorithm with a radius parameter of $R = 1.0$. In order to mitigate the effects from pile-up and the underlying event, a trimming procedure [25] is applied: constituents are clustered into subjets using the k_t algorithm [26] with $R_{\mathrm{sub}} = 0.2$, and any subjets that carry a fraction of the large-R jet's p_{T} of $p_{\mathrm{T}}^{\mathrm{subjet}}/p_{\mathrm{T}}^{\mathrm{jet}} < f_{\mathrm{cut}} = 0.05$ are removed. Tracks that are ghost-associated [27] to subjets after trimming are considered to be associated with the large-R jet.

A calibration is applied to standard large-R jets that corrects both the jet energy [28] and mass [3]. Both calibrations are determined by using the response with respect to particle-level trimmed truth jets in MC.

In addition to standard large-R jets, two new algorithms that reconstruct large-R ($R = 1.0$) jets by reclustering [29] small-R ($R = 0.2$) jets and tracks are defined in Section 5. These algorithms are the primary focus of the performance studies presented in this document.

Large-R jets are required to have $p_{\mathrm{T}} > 200$ GeV and $|\eta| < 2.0$. Only large-R jets that are matched to a reference truth jet described in Section 4.4 and that pass the truth classification described in Section 4.5 are used. QCD jets are required to be matched to a reference truth jet with $m^{\mathrm{true}} > 50$ GeV.

4.4 Truth jets

Stable truth particles with $c\tau > 10$ mm, excluding neutrinos and muons, are used to construct particle-level truth jets that serve as a reference to measure the detector response to jet observables and the corresponding resolutions. Throughout this document, trimmed anti-k_t large-R truth jets with $p_{\mathrm{T}} > 120$ GeV and $|\eta| < 2.4$ are used as a reference. They are reconstructed using the same algorithm as standard detector-level large-R jets, including the trimming parameters. In order for a truth jet to be considered as a reference for a detector-level jet, they are required to lie within $\Delta R < 0.2$ of each other. Other types of large-R truth jets were studied as reference jets, however, trimmed anti-k_t large-R truth jets were found to give consistent, albeit slightly worse resolutions and are therefore used for consistency with previous publications. The worsening of the resolutions can be understood as a result of the algorithm applied at truth level being is not the same as the one applied at detector level.

4.5 Truth-level classification of large-R jets

In order to study the performance of substructure algorithms on various jet topologies, all detector-level large-R jets are classified using truth information. The truth particles used in the classification are generator-level particles that have all radiative corrections applied, but have not yet decayed or hadronized. The truth particles used in the classification include top quarks, b-quarks, Higgs bosons, and W bosons.

Detector-level jets are classified as W jets, top jets, $H \to bb$ jets, $H \to WW^*$ jets, or QCD jets. Jets from the $W' \to WZ$ MC samples that are matched to a truth W boson and its two child quarks by ghost-association are classified as W jets. Jets from the $G^*_{KK} \to H(bb)H(bb)$ MC samples to which a truth Higgs boson and its two truth child b-quarks are ghost-associated are classified as $H \to bb$ jets. Similarly, jets from the $X \to H(WW^*)H(WW^*)$ MC samples that are matched via ghost-association to a truth Higgs boson, its two truth child W bosons, and the four child quarks of the W bosons are classified as $H \to WW^*$ jets. Jets from the $Z' \to tt$ MC samples are classified as top jets if they are matched via ghost-association to a truth top quark and its truth children, a W boson and a b-quark, and the two child quarks of the W boson. The classification efficiency is very high for all four topologies. All jets that come from the dijet samples are classified as QCD jets.

4.6 Standard jet mass observables

For a given large-R jet J, the mass is calculated from the four-vectors of their constituent objects, i:

$$m = \sqrt{\left(\sum_{i \in J} E_i\right)^2 - \left(\sum_{i \in J} \vec{p}_i\right)^2}. \tag{1}$$

Several different mass definitions are used for standard large-R jets [3]. The calorimeter mass, m^{calo}, is calculated using the constituent topological clusters, which are assumed to be massless. The track mass, m^{trk}, is calculated using tracks, which are assumed to have a mass of $m_{\pi^\pm}$, that are ghost-associated to the jet as constituents. In addition to these nominal mass definitions, two additional mass definitions are used in ATLAS that make use of both tracking and calorimeter information.

The track-assisted mass [3], m^{TA}, is defined as

$$m^{\mathrm{TA}} = \frac{p_{\mathrm{T}}^{\mathrm{calo}}}{p_{\mathrm{T}}^{\mathrm{trk}}} \times m^{\mathrm{trk}}$$

where $p_{\mathrm{T}}^{\mathrm{calo}}$ is the calibrated p_{T} of the large-R jet and $p_{\mathrm{T}}^{\mathrm{trk}}$ is the vector summed p_{T} of the ghost-associated tracks. This accounts for the energy missing in m^{trk} due to neutral particles on a jet-by-jet basis, the limiting factor for m^{trk}. The advantage of m^{TA} over m^{calo}, which is limited in its ability to resolve the angular information due to the finite size of topological clusters, is the usage of the information from the tracker that provides a superior angular resolution.

In order to further improve the resolution of the large-R jet mass, the combined mass [3], m^{comb}, is used. This makes use of the fact that m^{calo} provides a good resolution for low-p_{T} jets and m^{trk} provides a good resolution for high-p_{T} jets. The two mass observables are combined to form m^{comb} as an inverse-resolution weighted mean using the expected jet mass resolutions determined from MC simulations. As a result, the m^{comb} algorithm provides a superior resolution and is used as the standard large-R jet mass observable in ATLAS.

4.7 Other jet substructure observables

The N-subjettiness variables, τ_N [30, 31], make use of every jet constituent to distinguish between different jet topologies. This is done by measuring how well a jet is described as containing at least N subjets and the ratio τ_M/τ_N can be used to distinguish jets containing a specific number of subjets. It has been shown that τ_{21} is effective for identifying W jets [32], τ_{32} is effective for identifying top jets [33], and τ_{42} is effective for identifying $H \to WW^*$ jets [34]. All τ_N quantities used in this study use the Winner Takes All (WTA) axis, i.e., each subjet axis is defined by its hardest constituent instead of a vector sum of all of its constituents [35].

A class of variables known as Energy Correlation Functions, ECF(N,β) [36], and ratios of ECFs, C_2^{β} [37] and D_2^{β} [38], are used to describe the transverse energy distribution within a jet. It has been shown that $D_2^{\beta=1}$ is particularly effective for identifying two-body decays, such as W jets [32].

5 Track-assisted jet algorithm definitions

This section presents three alternative algorithms that make use of information from the tracker and the calorimeter to calculate jet substructure observables beyond the standard approaches discussed in Section 4. While the first algorithm has been previously investigated by ATLAS [3], the other two are newly developed approaches based on the reclustering technique [39], and were found in a systematic performance scan of about 20 candidate jet algorithm definitions. A summary of the three algorithms is shown in Figure 1.

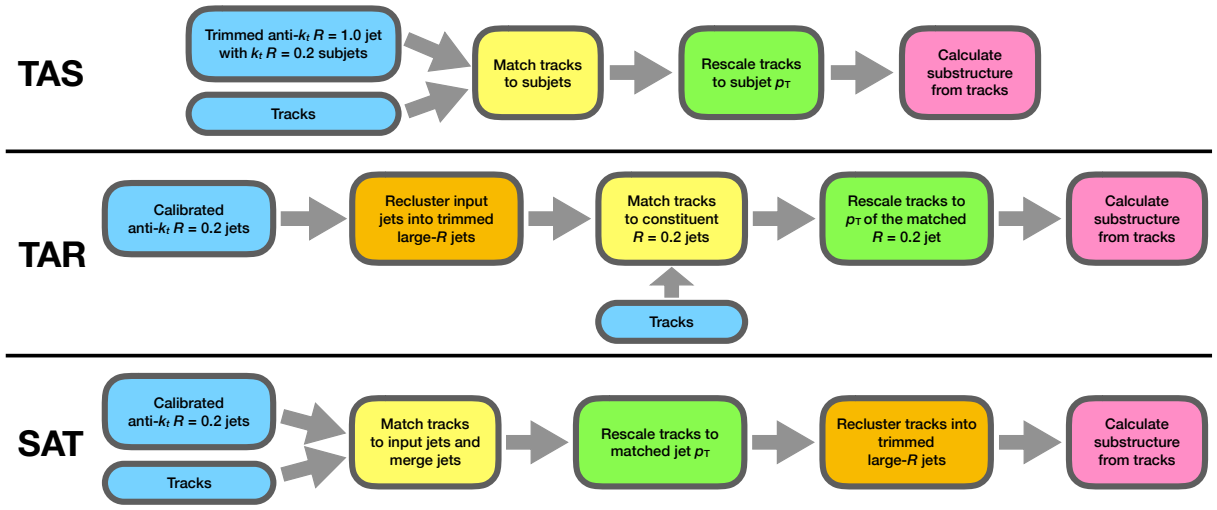

Figure 1: Flowchart summarising the TAS, TAR, and SAT algorithms. The inputs for each algorithm are listed in the blue boxes.

5.1 Track-assisted subjet algorithm (TAS)

The track-assisted subjet (TAS) algorithm [3] uses tracks whose p_{T} is scaled using calorimeter information to calculate mass and other substructure observables for standard large-R jets. Tracks that are ghost-associated with the standard large-R jet are matched to k_t subjets using ghost-association and any tracks that remain are matched to the nearest subjet in ΔR if $\Delta R_{\mathrm{subjet,track}} < 0.3$. The energy of neutral hadronic components is accounted for by scaling the p_{T} of all tracks as

$$p_{\mathrm{T}}^{\mathrm{track,\,new}} = p_{\mathrm{T}}^{\mathrm{track,\,old}} \times \frac{p_{\mathrm{T},j}^{\mathrm{subjet}}}{\sum_{i \in j} p_{\mathrm{T},i}^{\mathrm{track,\,old}}}, \tag{2}$$

where the index i runs over all tracks matched to subjet j. The rescaled tracks are clustered using the anti-k_t algorithm to form a single large-R jet. The mass, m^{TAS}, and other substructure observables of this jet are calculated directly using the momentum-corrected constituent tracks. The advantage of the TAS algorithm over the standard track-assistance is that it applies the correction for the missing fraction of the energy due to neutral particles on a subjet-by-subjet basis rather than on a jet-by-jet basis, thus accounting for local effects and resulting in a significantly improved substructure resolution. The TAS procedure, with a focus on m^{TAS}, is discussed in more detail in Ref. [3].

5.2 Track-assisted reclustered jet algorithm (TAR)

The track-assisted reclustered (TAR) jet algorithm uses tracks and calibrated anti-k_t $R = 0.2$ jets to reconstruct large-R anti-k_t jets. The $R = 0.2$ jets are clustered to form large-R jets that are then trimmed using $f_{\mathrm{cut}} = 0.05$. Optimization studies show that trimming improves the resolution of the TAR algorithm, despite using pile-up corrected $R = 0.2$ jets as input. Tracks are then matched to $R = 0.2$ jets that remain in the event after the trimming procedure is applied. This is done first using ghost-association and then

any remaining un-matched tracks are assigned to the nearest $R = 0.2$ jet if the jet axis lies within $\Delta R < 0.3$ of the track. The value of $\Delta R < 0.3$ was found to be optimal in terms of jet mass resolution for W jets. Following the matching procedure, the p_{T} of each constituent track is scaled using the p_{T} of the constituent jet to which it is matched, j, following Eq. 2. A large-R jet is then built from $R = 0.2$ jets with rescaled associated tracks and is referred to in the following as a TAR jet, the $R = 0.2$ jets from which the TAR jet is built are referred to as the constituent jets, and the tracks that are matched to the constituent jets are referred to as constituent tracks. The mass, m^{TAR}, and other substructure observables are calculated using these constituent tracks. The TAR algorithm provides all the advantages of the TAS approach. Furthermore, the TAR algorithm provides a straightforward method to calibrate and assign uncertainties to jet observables by propagating calibrations and uncertainties from the well-defined constituent $R = 0.2$ jets and tracks in what is referred to as bottom-up propagation of uncertainties.

5.3 Small-R jet assisted track algorithm (SAT)

The TAR algorithm is the most intuitive approach to using $R = 0.2$ jets and tracks to construct large-R jets, but a second simple approach is possible. The small-R jet assisted track (SAT) algorithm differs from the TAR algorithm in what objects are used as inputs to the initial large-R jet clustering. In its simplest form, tracks are matched to $R = 0.2$ jets and scaled following Eq. 2. The tracks are then clustered into large-R jets and trimming is applied to sub-jets built from the constituent tracks with the parameters $R_{\mathrm{sub}} = 0.2$ and $f_{\mathrm{cut}} = 0.05$. Jet substructure observables, including the mass m^{SAT}, are calculated from the constituent tracks.

This basic SAT algorithm has the disadvantage that any tracks that are matched to a soft radiation jet can be scaled to a low p_{T} and consequently be removed in the trimming procedure. In order to mitigate this, the SAT algorithm is modified as follows. Tracks are matched to $R = 0.2$ jets via ghost-association. If a $R = 0.2$ jet lies within $\Delta R_{\mathrm{jet,neighbor}} < 0.25$ of its nearest neighbor jet and has $p_{\mathrm{T}}/p_{\mathrm{T}}^{\mathrm{neighbor}} < 0.1$, which is characteristic of soft radiation jets, its four-momentum is added to the neighbor, resulting in a "merged" jet. The tracks assigned to each of the original $R = 0.2$ jets are matched to the merged jet. These tracks are scaled following Eq. 2 and then clustered into large-R jets and trimmed. The SAT algorithm provides all the advantages of the TAR approach and is found to have a very similar performance. Therefore, individual performance plots for the SAT algorithm are not shown in this document, and its performance is summarised in Table 1 together with the other algorithms.

6 Performance of jet substructure observables

Two different figures of merit are used to evaluate the performance of each jet algorithm. The first compares representative substructure observables, including mass, of detector-level jets to reference truth jets. The second compares the performance of the jet algorithms discriminating signal jets from background jets using basic selections on substructure observables.

In order to study fully contained heavy resonance decays with sufficient statistics, W jets are required to have 200 GeV $< p_{\mathrm{T}} <$ 2500 GeV, $H \to bb$ jets are required to have 250 GeV $< p_{\mathrm{T}} <$ 2000 GeV, top jets are required to have 450 GeV $< p_{\mathrm{T}} <$ 2500 GeV, and $H \to WW^*$ jets are required to have 250 GeV $< p_{\mathrm{T}} <$ 1500 GeV. QCD jets are required to have 200 GeV $< p_{\mathrm{T}} <$ 2500 GeV.

To avoid a potential bias, large-R jets are assigned weights such that each class of jets produces a flat distribution in p_{T} and $|\eta|$ in the full p_{T} range and $|\eta| < 2.0$. This is done to eliminate effects from differing p_{T} and $|\eta|$ distributions in the different MC samples.

6.1 Response of substructure observables

In the following, the performance of the standard and new jet algorithms is quantified using the response of detector-level jets relative to truth reference jets. A truth jet is considered the reference jet for a reconstructed jet if the two are separated by $\Delta R < 0.2$.

The response, $\mathcal{R}_x$, of observable x is either defined as

$$\mathcal{R}(x) = \frac{x_{\mathrm{reco}}}{x_{\mathrm{true}}}$$

if x is a dimensional quantity, such as jet mass or the k_t-splitting scale, or as

$$\mathcal{R}(x) = x_{\mathrm{reco}} - x_{\mathrm{true}}$$

if x is a dimensionless quantity, such as N-subjettiness or energy correlation ratios. In these definitions, x_{reco} is the reconstructed jet observable and x_{true} the reference truth jet observable.

The performance of each observable is quantified, as a function of p_{T}, by the median of the response distribution and by its width, defined using the interquantile range (IQnR) method [3]. The width of dimensionless quantities is defined as one half of the 50% IQnR and the width of dimensional quantities is defined as the 68% IQnR divided by twice the median. This width is referred to as "resolution" in the following.

Median response and calibrations

The median of the response for an observable indicates how well the observable is reconstructed in simulation. A calibration can be applied to compensate for deviations away from the ideal case for some observables, such as large-R jet p_{T} and mass. Substructure observables other than the jet mass are not calibrated.

A comparison of the median response for mass and $D_2^{\beta=1}$ as a function of p_{T} for W jets is shown in Figure 2. Calibrations are applied for m^{comb}, and the median response lies within at most 5% of unity, as the calibration is derived from a sample of QCD multijet events. In the TAR algorithm, calibrations are applied to the $R = 0.2$ jets, and are propagated to the m^{TAR} observable. Consequently, its median response lies within at most 5% of unity. No calibrations are applied to k_t subjets, so m^{TAS} underestimates the mass by $> 5\%$. An additional calibration, either on m^{TAS} or on k_t subjets could mitigate this.

Although the large-R jet mass can be calibrated, other substructure observables, such as $D_2^{\beta=1}$, are currently not calibrated in ATLAS. Therefore, the median response provides an important measure of how uniform the detector response to a given observable is as a function of p_{T}. While the median response of $D_2^{\beta=1}$ notably increases with p_{T} up to 0.5 for the standard jet algorithm, it is below 0.05 for the track-assisted

algorithms throughout the entire p_{T} range considered. Similar trends are observed for the median response for other jet topologies and other substructure observables.

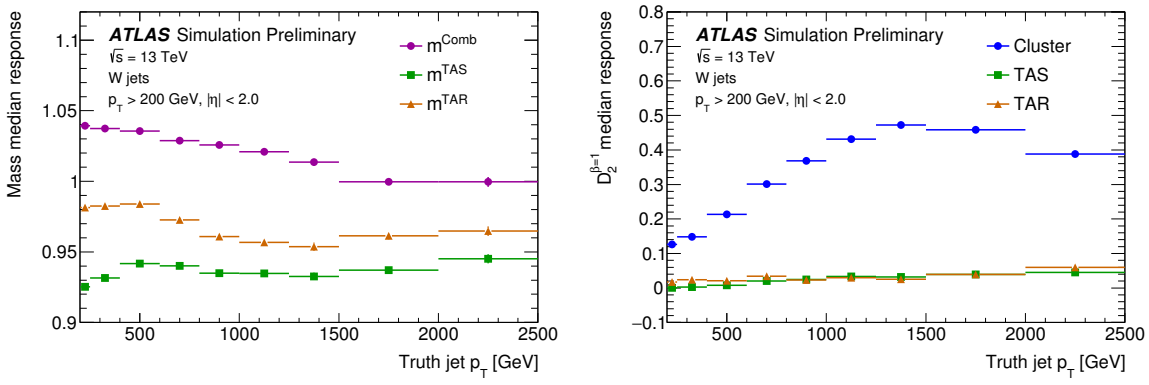

(a) (b)

Figure 2: Median response of mass (a) and $D_2^{\beta=1}$ (b) as a function of truth jet p_{T} for W jets. The figures of merit of the TAS and TAR jet reconstruction algorithms are compared to those of standard approaches, m^{comb} and $D_2^{\beta=1}$.

Mass resolution

The resolutions of the various large-R jet mass definitions are shown in Figure 3 for W, $H \to bb$, top, and $H \to WW^*$ topologies. These topologies are representative of hadronic decays into two, three, and four particles (prongs) in the leading-order picture. As a reference, resolutions for large-R jets in QCD multijet events are given in Figure 3(e).

While the median of the response quantifies the reconstruction quality of an observable, the resolution provides a useful metric for the experimental limitation of measuring the invariant mass of hadronically decaying resonances. Both m^{TAR} and m^{SAT} provide a better resolution than m^{comb} for low- to mid-range values of p_{T}.

- For W jets, m^{TAR} has the best resolution for $p_{\mathrm{T}} < 800$ GeV. A maximum relative gain of ~35% relative to m^{comb} is seen in the 200 GeV $< p_{\mathrm{T}} <$ 250 GeV bin. In the regime of $p_{\mathrm{T}} > 1500$ GeV, m^{TAR} again performs best among all the observables considered.
- For $H \to bb$ jets, m^{TAR} performs better than or similarly to m^{comb} for $p_{\mathrm{T}} < 1250$ GeV. A maximum relative gain of 35% is found in the 250 GeV $< p_{\mathrm{T}} <$ 400 GeV range.
- Similar trends are seen for top quark jets, where m^{TAR} performs best for $p_{\mathrm{T}} < 1000$ GeV with a maximum relative gain of 15%, and is comparable to m^{comb} at higher p_{T}.
- The performance is qualitatively similar for $H \to WW^*$ jets such that m^{TAR} performs best for $p_{\mathrm{T}} < 600$ GeV, with a maximum relative gain of 15%.
- The best resolution for QCD jets is seen in the $p_{\mathrm{T}} < 800$ GeV and 1500 GeV $< p_{\mathrm{T}} <$ 2500 GeV ranges with m^{TAR}, which gives a relative gain of 10% with respect to m^{comb}.

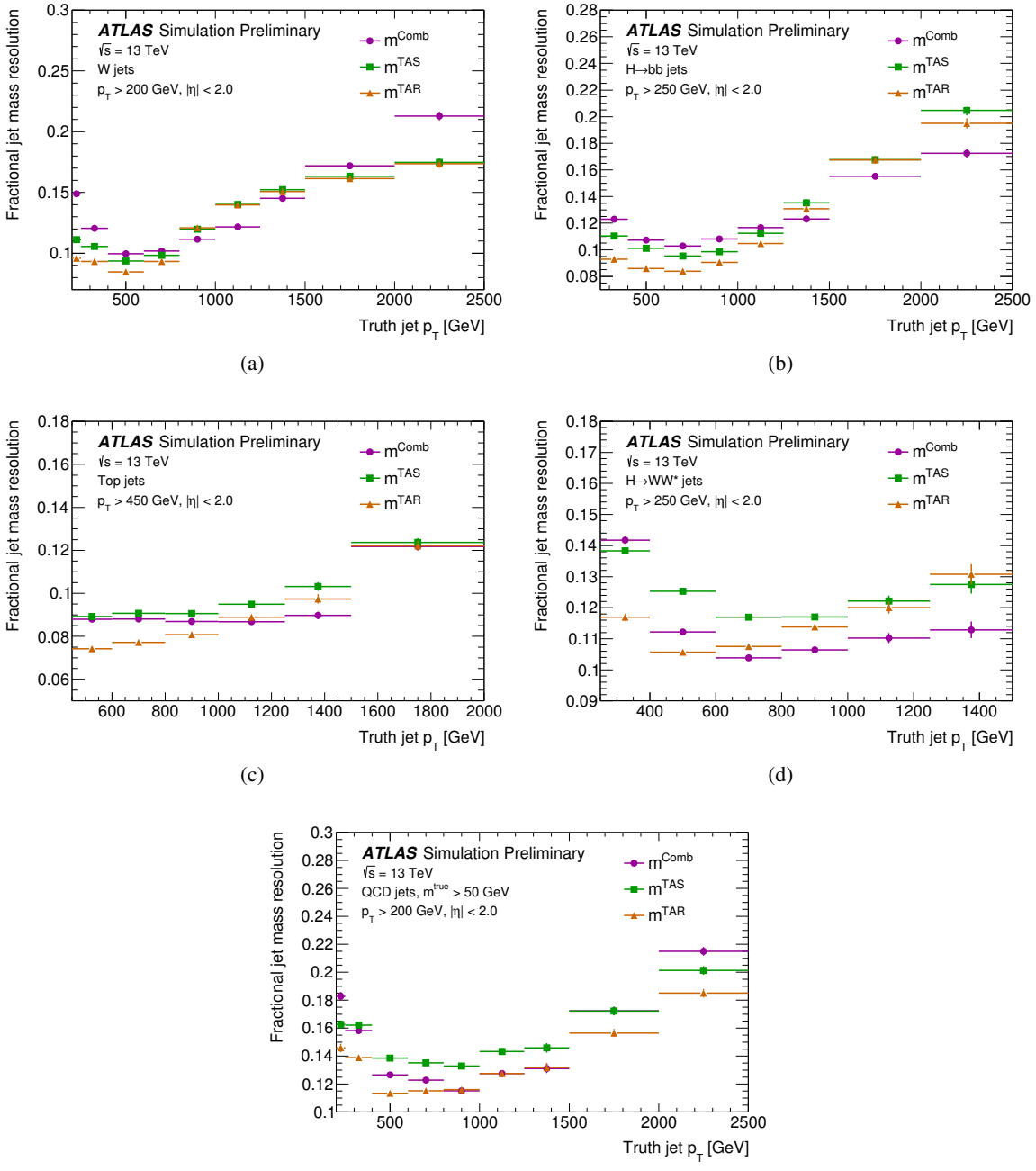

Figure 3: Large-R jet mass resolution as a function of truth jet p_{T} for W (a), $H \to bb$ (b), top (c), $H \to WW^*$ (d), and QCD jets (e). The TAS and TAR jet mass algorithms are compared to the standard jet mass algorithm, m^{comb}. For QCD jets, $m^{\mathrm{true}} > 50$ GeV is required.

The p_{T} ranges where m^{TAR} provides better performance can be understood by considering the masses of the decaying particles: for very high momenta compared to the mass of the resonance, $R = 0.2$ jets tend to merge, nullifying the gains from using a subjet as a proxy for the hadronization products of each quark from the decay. For Higgs jets, the merging begins at a lower p_{T} for $H \to WW^*$ decays than for $H \to bb$ decays due to the internal structure of four- instead of two-prong decays.

Resolution of other observables

The resolution of τ_{21}^{WTA} using the various jet substructure algorithms is shown for W and QCD jets in Figure 4. The resolution for the TAS and TAR algorithms is significantly improved compared to standard large-R jets, and deteriorates much more slowly with increasing p_{T}. The relative gain in resolution increases with p_{T} and reaches 45% for W jets and 30% for QCD jets for $p_{\mathrm{T}} > 2000$ GeV. The resolution provided by track-assisted jet algorithms is $< 5\%$ for W jets with $p_{\mathrm{T}} < 800$ GeV and for QCD jets with $p_{\mathrm{T}} < 1500$ GeV.

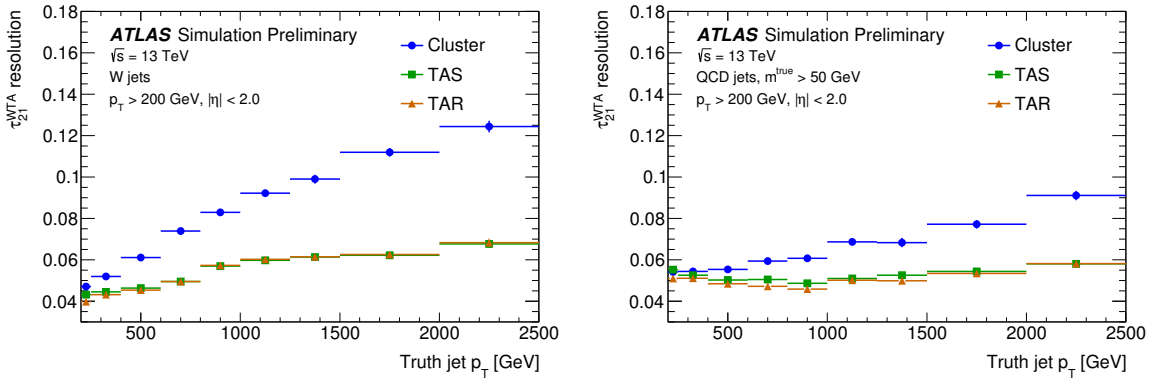

(a) (b)

Figure 4: Resolution of τ_{21}^{WTA} for W (a) and QCD jets (b) as a function of truth jet p_{T}. The TAS and TAR jet reconstruction algorithms are compared to the standard algorithm labeled as "Cluster". For QCD jets, $m^{\mathrm{true}} > 50$ GeV is required.

The resolution of $D_2^{\beta=1}$ follows the same trend as τ_{21}^{WTA} as shown in Figure 5 for W, $H \to bb$, and QCD jets. TAS and TAR jets all have improved resolutions compared to standard large-R jets with the best resolution coming from the TAR algorithm. The relative gain in resolution is 50% for W jets, 30% for $H \to bb$ jets with $p_{\mathrm{T}} > 1500$ GeV, and 25% for QCD jets with 1000 GeV $< p_{\mathrm{T}} < 1500$ GeV. As for τ_{21}^{WTA}, the relative gain increases with p_{T} for W and $H \to bb$ jets.

The resolution of τ_{32}^{WTA} for top and QCD jets is shown in Figure 6. Both track-assisted algorithms provide significantly improved τ_{32}^{WTA} resolutions compared to standard large-R jets throughout the entire kinematic range considered. The relative gain in the resolution can be as high as 15% for top jets and 60% for QCD jets. The resolution degrades only mildly with p_{T} because of the larger opening angle of the decay products compared to e.g., W jets, due the large top quark mass. The resolution for QCD jets remains mostly constant throughout the entire p_{T} range.

The four-prong topology is shown in Figure 7, which shows the resolution of τ_{42}^{WTA} for $H \to WW^*$ jets. Similarly to the two- and three-prong topologies, the track-assisted algorithms outperform standard jets

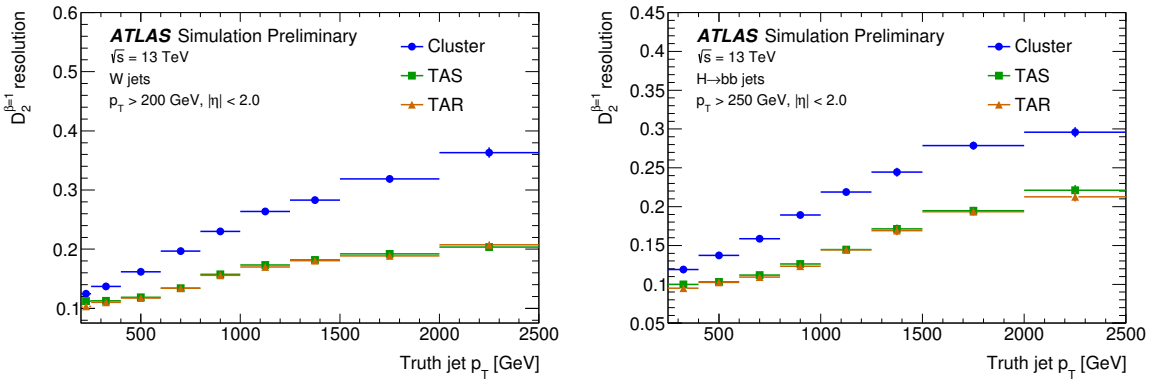

(a)

(b)

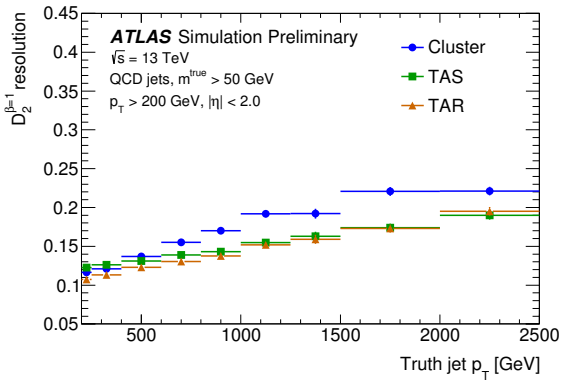

(c)

Figure 5: Resolution of $D_2^{\beta=1}$ for W (a), $H \to bb$ (b), and QCD jets (c) as a function of truth jet p_{T}. The TAS and TAR jet reconstruction algorithms are compared to the standard algorithm labeled as "Cluster". For QCD jets, $m^{\mathrm{true}} > 50$ GeV is required.

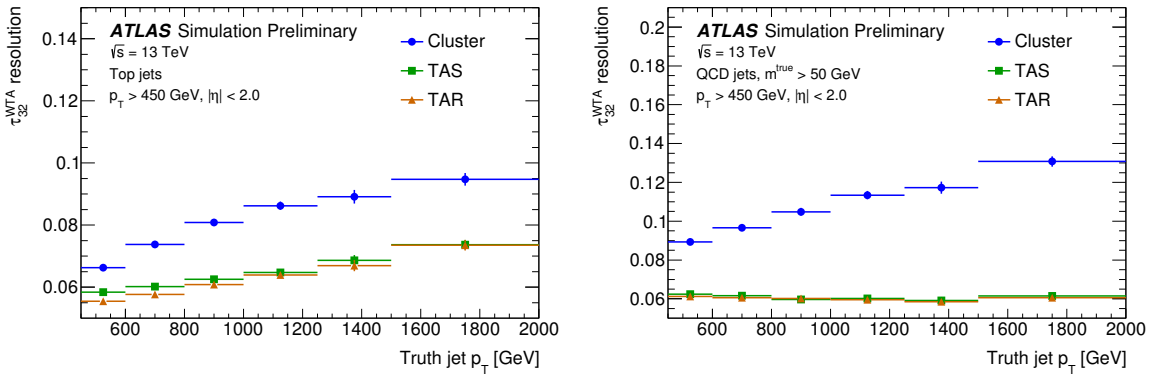

(a)

(b)

Figure 6: Resolution of τ_{32}^{WTA} for top (a) and QCD jets (b) as a function of truth jet p_{T}. The TAS and TAR jet reconstruction algorithms are compared to the standard algorithm labeled as "Cluster". For QCD jets, $m^{\mathrm{true}} > 50$ GeV is required.

across the full kinematic range studied. The best relative resolution of 6% is obtained for both $H \to WW^*$ and QCD jets and remains approximately constant for TAS and TAR jets while it deteriorates to 10% and 15% with increasing p_{T} for standard jets. The relative improvement in the resolution obtained with track-assisted algorithms relative to standard jets increases with p_{T} and is most dramatic for four-prong topologies shown here, and can be as large as 35% for $H \to WW^*$ jets and 60% for QCD jets.

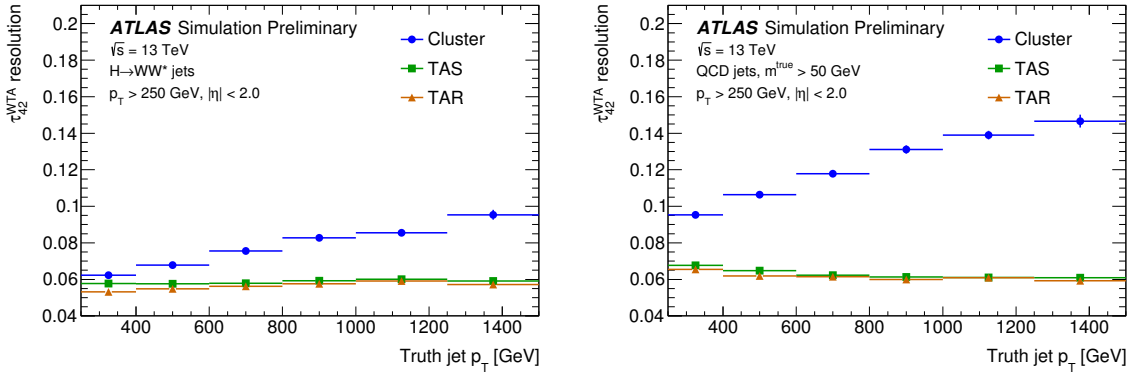

(a) (b)

Figure 7: Resolution of τ_{42}^{WTA} for $H \to WW^*$ (a) and QCD jets (b) as a function of truth jet p_{T}. The TAS and TAR jet reconstruction algorithms are compared to the standard algorithm labeled as "Cluster". For QCD jets, $m^{\mathrm{true}} > 50$ GeV is required.

6.2 Tagging heavy resonances

The second figure of merit for comparing the performance of the different jet algorithms is the effectiveness in distinguishing jets from heavy resonance decays from jets from QCD multijet events using the mass and other substructure observables of a jet. Sophisticated methods have been developed to identify W [40], $H \to bb$ jets [41], and top jets [40], but two-variable taggers are used as proxies to demonstrate the relative performance gains of each jet algorithm. The tagging variables for each topology are used with a requirement on the smallest mass window which is 68% efficient for signal jets. In the case of standard large-R jet observables, the mass window cut is applied on m^{comb} and for TAS and TAR, the mass window cut is applied on the corresponding mass variable.

The effectiveness of each tagger can be seen using Receiver Operator Characteristic (ROC) curves that measure background rejection, defined as $\frac{1}{\epsilon_{\mathrm{bkg}}}$, as a function of signal efficiency, ϵ_{sig}. The denominator in the efficiency calculations is defined using the weighted number of jets with $p_{\mathrm{T}} > 200$ GeV for QCD and W jets, 250 GeV for $H \to bb$ and $H \to WW^*$ jets, and 450 GeV for top jets, $m^{\mathrm{true}} > 50$ GeV for QCD jets, $|\eta| < 2.0$, and pass the truth classification criteria described in Section 4.5. The numerator is defined in the same way as the denominator with the addition of cuts on a mass window and, except for $H \to bb$ identification, the tagging variable. ROC curves represent a compact method of comparing the relative performance of various tagging configurations. Another, simpler metric is given by the background rejection for a working point (WP) corresponding to signal efficiency of 50%. In the following, the tagging effectiveness is studied for W, $H \to bb$, top, and $H \to WW^*$ jets using QCD multijet events as background. ROC curves are shown for low- and high-p_{T} ranges to demonstrate the p_{T} dependence of the tagging variables.

The effectiveness of tagging W jets with τ_{21}^{WTA} and $D_2^{\beta=1}$ is shown in the ROC curves in Figure 8 for 200 GeV $< p_{\mathrm{T}} <$ 600 GeV and 600 GeV $< p_{\mathrm{T}} <$ 2500 GeV. Both observables show similar trends. Both track-assisted algorithms result in nearly identical ROC curves and in a significant improvement compared to standard large-R jets. The best background rejection is seen for TAR jets with a p_{T} inclusive improvement of ~40% using τ_{21}^{WTA} and ~100% using $D_2^{\beta=1}$. The increased gain when using $D_2^{\beta=1}$ instead of τ_{21}^{WTA} is shown to come from the high-p_{T} region.

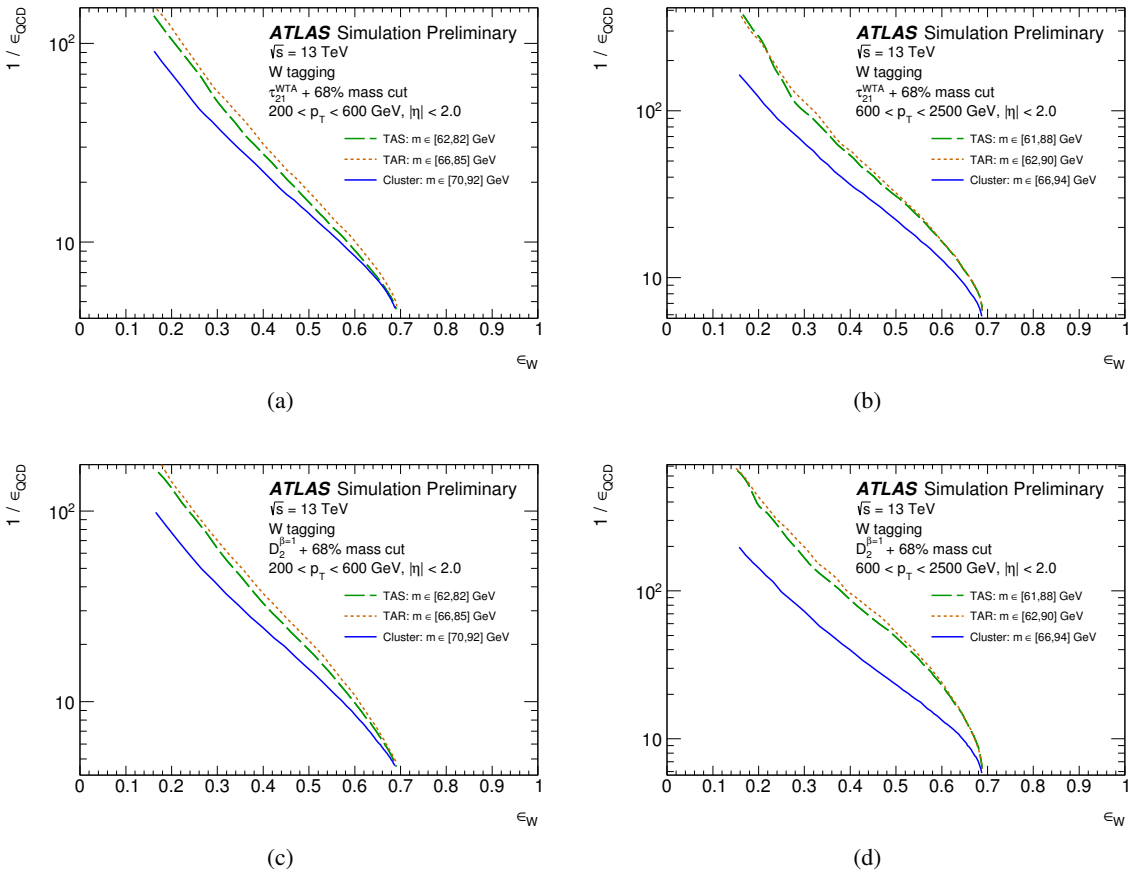

Figure 8: ROC curves comparing the separation power of a 68% efficient mass window cut plus either τ_{21}^{WTA} or $D_2^{\beta=1}$ in distinguishing W jets from QCD jets. Track-assisted jet reconstruction algorithms, TAS and TAR, are compared to the standard algorithm labeled as "Cluster". The τ_{21}^{WTA} separation is shown for 200 GeV $< p_{\mathrm{T}} <$ 600 GeV (a) and 600 GeV $< p_{\mathrm{T}} <$ 2500 GeV (b), while the respective distributions for $D_2^{\beta=1}$ are shown in (c) and (d). The mass window range in units of GeV is indicated for each algorithm in the legend. When calculating ϵ_{QCD}, $m^{\mathrm{true}} > 50$ GeV is required. The signal and background samples are weighted to have flat p_{T} and $|\eta|$ spectra.

Unlike other topologies, it has been shown that the identification of b quark jets (b-tagging) is the best discriminant for identifying $H \to bb$ jets. Jet mass requirements provide further discrimination, but other substructure variables are shown to contribute little additional gain [41]. Therefore, ROC curve comparisons using only mass observables for $H \to bb$ jets are shown in Figure 9. The three mass definitions, m^{comb}, m^{TAS}, and m^{TAR} produce very similar ROC curves with a slight loss in performance for m^{TAR} at high p_{T}.

The effectiveness of using τ_{32}^{WTA} to tag top jets is shown using ROC curves in Figure 10. The ROC curves

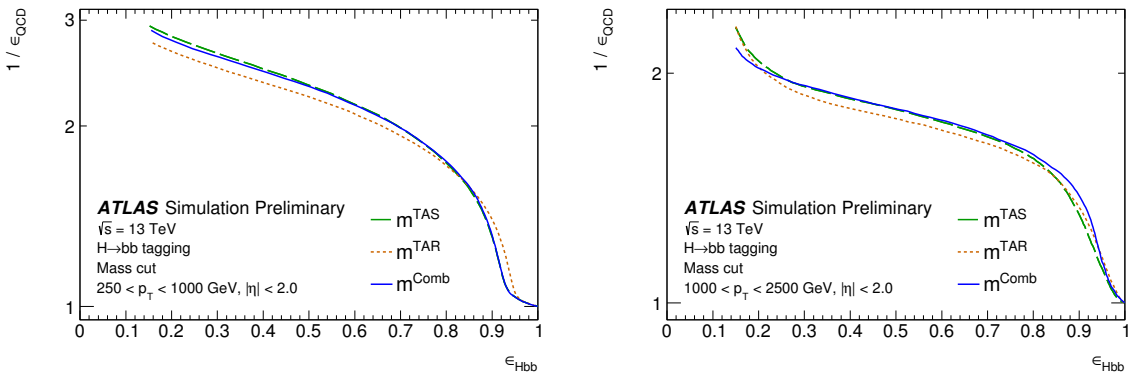

(a) (b)

Figure 9: ROC curves comparing the separation power of jet mass in distinguishing $H \to bb$ jets from QCD jets. Track-assisted jet mass definitions, m^{TAS} and m^{TAR}, are compared to the standard mass definition m^{comb}. The mass separation is shown for 250 GeV $< p_{\text{T}} <$ 1000 GeV (a) and 1000 GeV $< p_{\text{T}} <$ 2500 GeV (b). No b-tagging requirement is applied. When calculating ϵ_{QCD}, $m^{\text{true}} > 50$ GeV is required. The signal and background samples are weighted to have flat p_{T} and $|\eta|$ spectra.

for both track-assisted algorithms are nearly identical and show significant improvements compared to standard large-R jets. The improvement increases for high-p_{T} jets.

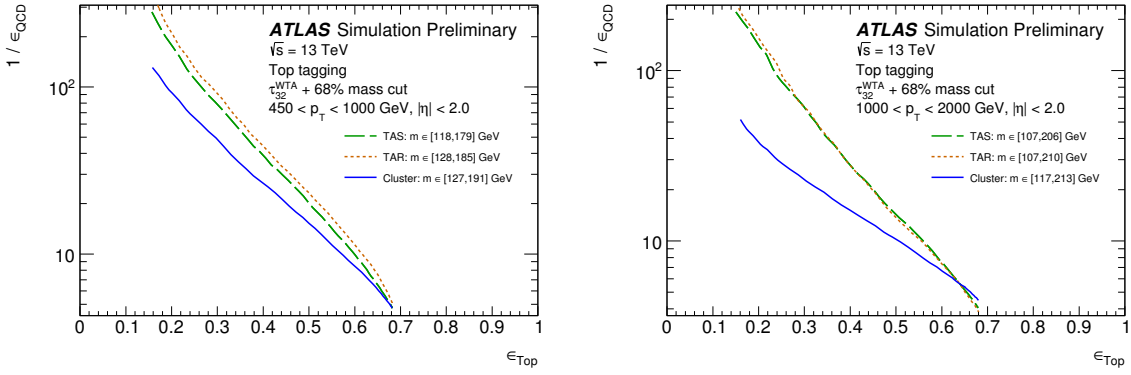

(a) (b)

Figure 10: ROC curves comparing the separation power of a 68% efficient mass window cut plus τ_{32}^{WTA} in distinguishing top jets from QCD jets. Track-assisted jet reconstruction algorithms, TAS and TAR, are compared to the standard algorithm labeled as "Cluster". The τ_{32}^{WTA} separation is shown for 450 GeV $< p_{\text{T}} <$ 1000 GeV (a) and 1000 GeV $< p_{\text{T}} <$ 2000 GeV (b). The mass window range in units of GeV is indicated for each algorithm in the legend. When calculating ϵ_{QCD}, $m^{\text{true}} > 50$ GeV is required. The signal and background samples are weighted to have flat p_{T} and $|\eta|$ spectra.

Figure 11 compares the ROC curves for using τ_{42}^{WTA} to tag $H \to WW^*$ jets. Similar to tagging top jets with τ_{32}^{WTA}, both track-assisted algorithms result in nearly identical ROC curves that are significantly improved compared to standard large-R jets, increasingly so at high-p_{T}.

The tagging performance for the various processes and jet substructure observables is summarized in Table 1 as background rejection at a 50% signal efficiency WP for large-R jets with $p_{\text{T}} > 200$ GeV for W

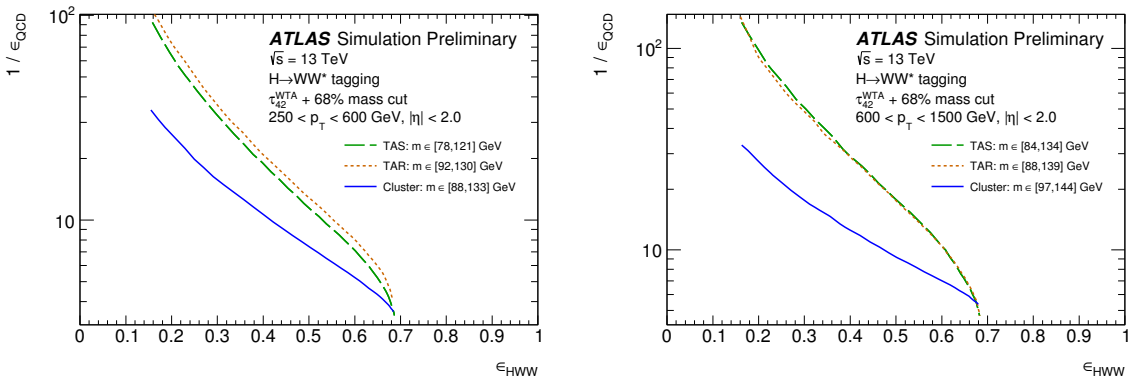

(a) (b)

Figure 11: ROC curves comparing the separation power of a 68% efficient mass window cut plus τ_{42}^{WTA} in distinguishing $H \to WW^*$ jets from QCD jets. Track-assisted jet reconstruction algorithms, TAS and TAR, are compared to the standard algorithm labeled as "Cluster". The τ_{42}^{WTA} separation is shown for 250 GeV $< p_{\mathrm{T}} <$ 600 GeV (a) and 600 GeV $< p_{\mathrm{T}} <$ 1500 GeV (b). The mass window range in units of GeV is indicated for each algorithm in the legend. When calculating ϵ_{QCD}, $m^{\mathrm{true}} > 50$ GeV is required. The signal and background samples are weighted to have flat p_{T} and $|\eta|$ spectra.

jets, 250 GeV for $H \to bb$ and $H \to WW^*$ jets, and 450 GeV for top jets. The background rejection as a function of large-R jet p_{T} for a 50% signal efficient WP is shown in Fig. 12.

Process	Observable	Algorithm	$1/\epsilon_{\mathrm{QCD}}$		
			Mass only	Observable only	Mass + observable
W jets	τ_{21}^{WTA}	Cluster	9.1	3.1	18
		TAS	9.5	4.0	23
		TAR	9.6	**4.2**	**25**
		SAT	**10**	3.8	22
	$D_2^{\beta=1}$	Cluster	9.1	2.7	15
		TAS	9.5	4.5	30
		TAR	9.6	**4.7**	**32**
		SAT	**10**	4.4	27
$H \to bb$ jets	$D_2^{\beta=1}$	Cluster	7.7	2.8	10
		TAS	**7.8**	3.5	10
		TAR	7.7	**3.6**	**11**
		SAT	7.6	3.4	10
Top jets	τ_{32}^{WTA}	Cluster	**9.3**	3.6	12
		TAS	8.8	7.3	15
		TAR	8.6	**7.5**	**17**
		SAT	8.9	7.1	16
$H \to WW^*$ jets	τ_{42}^{WTA}	Cluster	**8.4**	2.5	8.3
		TAS	7.1	5.7	14
		TAR	8.0	**5.8**	**15**
		SAT	7.4	5.3	14

Table 1: Comparison of the rejection of QCD background jets for various observables to tag W, $H \to bb$, top, and $H \to WW^*$ jets for a signal tagging efficiency of 50% using a mass window requirement alone, only a jet substructure observable other than mass, and a 68% efficient mass window requirement combined with a selection on another jet substructure observable. No b-tagging requirement is applied. Track-assisted jet reconstruction algorithms TAS, TAR, and SAT are compared to the standard algorithm labeled as "Cluster". For the standard algorithm m^{comb} is used. The best background rejection for each signal and variable combination is given in bold. When calculating ϵ_{QCD}, $m^{\mathrm{true}} > 50$ GeV is required.

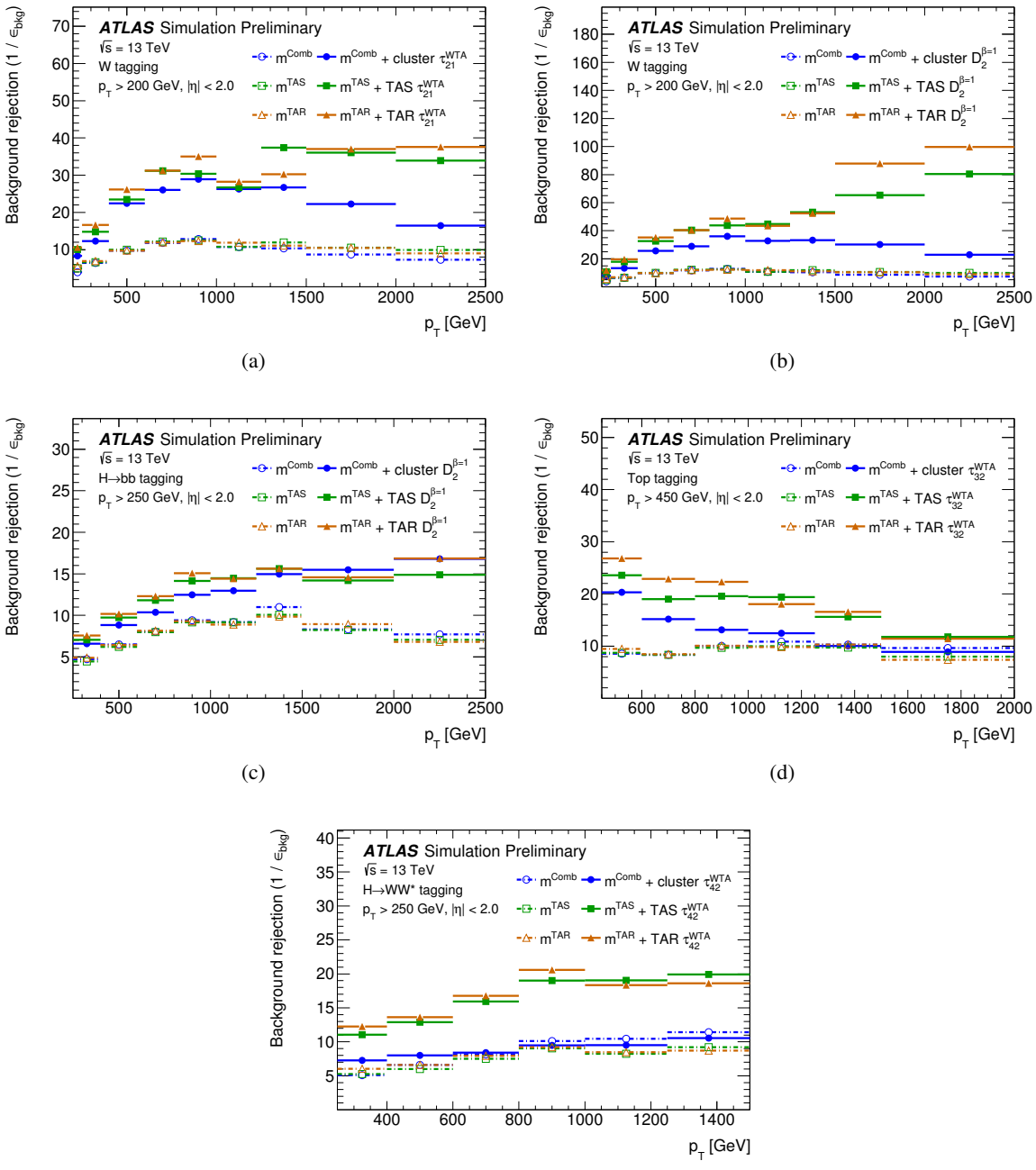

Figure 12: Background rejection for a signal efficiency of 50% as a function of large-R jet p_{T} for τ_{21}^{WTA} (a) and $D_2^{\beta=1}$ (b) applied to W jets, $D_2^{\beta=1}$ and $H \to bb$ jets (c), τ_{32}^{WTA} and top jets (d), as well as τ_{42}^{WTA} and $H \to WW^*$ jets (e). No b-tagging requirement is applied for $H \to bb$ tagging. The TAS and TAR algorithms are compared to m^{comb} and the combination of m^{comb} and other jet substructure observables calculated from calorimeter clusters. When calculating ϵ_{QCD}, $m^{\mathrm{true}} > 50$ GeV is required.

7 Conclusions

Two new approaches to reconstruct jet substructure observables using the information from the tracker and the calorimeters, the track-assisted reclustered (TAR) jet algorithm and the small-R jet assisted track (SAT) jet algorithm, are shown alongside the track-assisted subjet (TAS) algorithm. These approaches provide an improved sensitivity compared to substructure observables calculated only from calorimeter information due to additionally using information from the tracker, which provides a good angular resolution. The performance of jet substructure observables reconstructed with the TAS, TAR, and SAT algorithms is shown to be superior to calorimeter-only techniques in regions of kinematic phase space that are important to the identification of boosted, hadronically decaying heavy resonances. The TAR and SAT algorithms provide a similar performance, which is better than that provided by the TAS algorithm.

References

[1] L. Asquith et al., *Jet Substructure at the Large Hadron Collider : Experimental Review*, (2018), arXiv: 1803.06991 [hep-ex].

[2] A. J. Larkoski, I. Moult and B. Nachman, *Jet Substructure at the Large Hadron Collider: A Review of Recent Advances in Theory and Machine Learning*, (2017), arXiv: 1709.04464 [hep-ph].

[3] ATLAS Collaboration, *Jet mass reconstruction with the ATLAS Detector in early Run 2 data*, ATLAS-CONF-2016-035, 2016, URL: https://cds.cern.ch/record/2200211.

[4] S. Schaetzel and M. Spannowsky, *Tagging highly boosted top quarks*, Phys. Rev. **D89** (2014) 014007, arXiv: 1308.0540 [hep-ph].

[5] A. Katz, M. Son and B. Tweedie, *Jet Substructure and the Search for Neutral Spin-One Resonances in Electroweak Boson Channels*, JHEP **03** (2011) 011, arXiv: 1010.5253 [hep-ph].

[6] ATLAS Collaboration, *Improving jet substructure performance in ATLAS using Track-CaloClusters*, ATL-PHYS-PUB-2017-015, 2017, URL: https://cds.cern.ch/record/2275636.

[7] ATLAS Collaboration, *Jet reconstruction and performance using particle flow with the ATLAS Detector*, Eur. Phys. J. C **77** (2017) 466, arXiv: 1703.10485 [hep-ex].

[8] Sjöstrand, T., S. Mrenna and P. Z. Skands, *A Brief Introduction to PYTHIA 8.1*, Comput.Phys.Commun. **178** (2008) 852, arXiv: 0710.3820 [hep-ph].

[9] R. D. Ball, V. Bertone, S. Carrazza, C. S. Deans, L. Del Debbio et al., *Parton distributions with LHC data*, Nucl. Phys. **B867** (2013) 244, arXiv: 1207.1303 [hep-ph].

[10] ATLAS Collaboration, *ATLAS Pythia 8 tunes to 7 TeV data*, ATL-PHYS-PUB-2014-021, 2014, URL: https://cds.cern.ch/record/1966419.

[11] K. Agashe, H. Davoudiasl, G. Perez and A. Soni, *Warped Gravitons at the LHC and Beyond*, Phys. Rev. **D76** (2007) 036006, arXiv: hep-ph/0701186 [hep-ph].

[12] A. L. Fitzpatrick, J. Kaplan, L. Randall and L.-T. Wang,
Searching for the Kaluza-Klein Graviton in Bulk RS Models, JHEP **09** (2007) 013,
arXiv: hep-ph/0701150 [hep-ph].

[13] J. Alwall et al., *The automated computation of tree-level and next-to-leading order differential cross sections, and their matching to parton shower simulations*, JHEP **07** (2014) 079,
arXiv: 1405.0301 [hep-ph].

[14] J. Bellm et al., *Herwig++ 2.7 Release Note*, (2013), arXiv: 1310.6877 [hep-ph].

[15] J. Pumplin et al.,
New generation of parton distributions with uncertainties from global QCD analysis,
JHEP **07** (2002) 012, arXiv: hep-ph/0201195 [hep-ph].

[16] S. Gieseke, C. Rohr and A. Siodmok, *Colour reconnections in Herwig++*,
Eur. Phys. J. **C72** (2012) 2225, arXiv: 1206.0041 [hep-ph].

[17] ATLAS Collaboration, *The ATLAS Simulation Infrastructure*, Eur. Phys. J. C **70** (2010) 823,
arXiv: 1005.4568 [physics.ins-det].

[18] GEANT4 Collaboration, *GEANT4: A Simulation toolkit*, Nucl. Instrum. Meth. **A506** (2003) 250.

[19] ATLAS Collaboration,
Early Inner Detector Tracking Performance in the 2015 Data at $\sqrt{s}$ = 13 TeV,
ATL-PHYS-PUB-2015-051, 2015, URL: https://cds.cern.ch/record/2110140.

[20] ATLAS Collaboration, *The Optimization of ATLAS Track Reconstruction in Dense Environments*,
ATL-PHYS-PUB-2015-006, 2015, URL: https://cds.cern.ch/record/2002609.

[21] ATLAS Collaboration,
Topological cell clustering in the ATLAS calorimeters and its performance in LHC Run 1,
Eur. Phys. J. C **77** (2017) 490, arXiv: 1603.02934 [hep-ex].

[22] M. Cacciari, G. P. Salam and G. Soyez, *FastJet User Manual*, Eur. Phys. J. **C72** (2012) 1896,
arXiv: 1111.6097 [hep-ph].

[23] M. Cacciari, G. P. Salam and G. Soyez, *The Anti-k(t) jet clustering algorithm*,
JHEP **0804** (2008) 063, arXiv: 0802.1189 [hep-ph].

[24] ATLAS Collaboration, *Jet energy scale measurements and their systematic uncertainties in proton–proton collisions at $\sqrt{s}$ = 13 TeV with the ATLAS detector*,
Phys. Rev. D **96** (2017) 072002, arXiv: 1703.09665 [hep-ex].

[25] D. Krohn, J. Thaler and L.-T. Wang, *Jet Trimming*, JHEP **02** (2010) 084,
arXiv: 0912.1342 [hep-ph].

[26] S. Catani, Y. L. Dokshitzer, M. H. Seymour and B. R. Webber,
Longitudinally invariant K_t clustering algorithms for hadron hadron collisions,
Nucl. Phys. **B406** (1993) 187.

[27] M. Cacciari, G. P. Salam and G. Soyez, *The Catchment Area of Jets*, JHEP **04** (2008) 005,
arXiv: 0802.1188 [hep-ph].

[28] ATLAS Collaboration, *Monte Carlo Calibration and Combination of In-situ Measurements of Jet Energy Scale, Jet Energy Resolution and Jet Mass in ATLAS*, ATLAS-CONF-2015-037, 2015,
URL: https://cds.cern.ch/record/2044941.

[29] B. Nachman, P. Nef, A. Schwartzman, M. Swiatlowski and C. Wanotayaroj, *Jets from Jets: Re-clustering as a tool for large radius jet reconstruction and grooming at the LHC*, JHEP **02** (2015) 075, arXiv: 1407.2922 [hep-ph].

[30] J. Thaler and K. Van Tilburg, *Identifying Boosted Objects with N-subjettiness*, JHEP **03** (2011) 015, arXiv: 1011.2268 [hep-ph].

[31] J. Thaler and K. Van Tilburg, *Maximizing Boosted Top Identification by Minimizing N-subjettiness*, JHEP **02** (2012) 093, arXiv: 1108.2701 [hep-ph].

[32] ATLAS Collaboration, *Identification of Boosted, Hadronically Decaying W Bosons and Comparisons with ATLAS Data Taken at $\sqrt{s} = 8$ TeV*, Eur. Phys. J. C **76** (2016) 154, arXiv: 1510.05821 [hep-ex].

[33] ATLAS Collaboration, *Identification of high transverse momentum top quarks in pp collisions at $\sqrt{s} = 8$ TeV with the ATLAS detector*, JHEP **06** (2016) 093, arXiv: 1603.03127 [hep-ex].

[34] CMS Collaboration, *Search for a massive resonance decaying into a Higgs boson and a W or Z boson in hadronic final states in proton–proton collisions at $\sqrt{s} = 8$ TeV*, JHEP **02** (2016) 145, arXiv: 1506.01443 [hep-ex].

[35] A. J. Larkoski, D. Neill and J. Thaler, *Jet Shapes with the Broadening Axis*, JHEP **04** (2014) 017, arXiv: 1401.2158 [hep-ph].

[36] A. J. Larkoski, G. P. Salam and J. Thaler, *Energy Correlation Functions for Jet Substructure*, JHEP **06** (2013) 108, arXiv: 1305.0007 [hep-ph].

[37] A. J. Larkoski, I. Moult and D. Neill, *Power Counting to Better Jet Observables*, JHEP **12** (2014) 009, arXiv: 1409.6298 [hep-ph].

[38] A. J. Larkoski, I. Moult and D. Neill, *Analytic Boosted Boson Discrimination*, JHEP **05** (2016) 117, arXiv: 1507.03018 [hep-ph].

[39] ATLAS Collaboration, *Jet reclustering and close-by effects in ATLAS Run 2*, ATLAS-CONF-2017-062, 2017, URL: https://cds.cern.ch/record/2275649.

[40] ATLAS Collaboration, *Performance of Top Quark and W Boson Tagging in Run 2 with ATLAS*, ATLAS-CONF-2017-064, 2017, URL: https://cds.cern.ch/record/2281054.

[41] ATLAS Collaboration, *Boosted Higgs ($\to b\bar{b}$) Boson Identification with the ATLAS Detector at $\sqrt{s} = 13$ TeV*, ATLAS-CONF-2016-039, 2016, URL: https://cds.cern.ch/record/2206038.